communications materials

ARTICLE

https://doi.org/10.1038/s43246-022-00318-3 OPEN

Spectroscopic evidence of flat bands in breathing kagome semiconductor Nb_3I_8

Sabin Regmi[1], Tharindu Fernando[2], Yuzhou Zhao[2], Anup Pradhan Sakhya[1], Gyanendra Dhakal[1], Iftakhar Bin Elius[1], Hector Vazquez[1], Jonathan D. Denlinger[3], Jihui Yang[4], Jiun-Haw Chu[2], Xiaodong Xu[2], Ting Cao[4] & Madhab Neupane[1]✉

Kagome materials have become solid grounds to study the interplay among geometry, topology, correlation, and magnetism. Recently, niobium halide semiconductors Nb_3X_8 (X = Cl, Br, I) have been predicted to be two-dimensional magnets and these materials are also interesting for their breathing kagome geometry. However, experimental electronic structure studies of these promising materials are still lacking. Here, we report the spectroscopic evidence of flat and weakly dispersing bands in breathing-kagome semiconductor Nb_3I_8 around 500 meV binding energy, which is well supported by our first-principles calculations. These bands originate from the breathing kagome lattice of niobium atoms and have niobium *d*-orbital character. They are found to be sensitive to the polarization of the incident photon beam. Our study provides insight into the electronic structure and flat band topology in an exfoliable kagome semiconductor, thereby providing an important platform to understand the interaction of geometry and electron correlations in two-dimensional materials.

[1] Department of Physics, University of Central Florida, Orlando, FL 32816, USA. [2] Department of Physics, University of Washington, Seattle, WA 98195, USA. [3] Lawrence Berkeley National Laboratory, Berkeley, CA 94720, USA. [4] Department of Materials Science and Engineering, University of Washington, Seattle, WA 98195, USA. ✉email: madhab.neupane@ucf.edu

Owing to the possibility of exploring the interplay among some or all parameters, such as geometry, topology, electronic correlations and magnetism, quantum materials with kagome lattice have recently been attracting a bulk of research studies[1–10]. Comprised of corner-sharing triangles forming a hexagon within, a kagome lattice may feature a relativistic Dirac band crossing at the corner of the Brillouin zone (BZ)[11]. Because of the structural geometry, the electrons are trapped within the hexagon. This geometry-driven self-localization of the electrons means that flat bands may be present in the electronic structure of the kagome materials and give rise to strong electronic correlations[4,12–15]. By introducing spin–orbit coupling and magnetism that breaks the time-reversal symmetry, the Dirac band crossing at the corner of the BZ can be gapped out leading to intrinsic Chern quantum phases[8,16–18]. The band gap may be opened also when the alternating triangles in the kagome lattice have different bond lengths resulting in a different geometry than the conventional kagome (in which all the triangles are identical)—called the breathing kagome[19]—leading to the possibility of higher-order topological phase[20]. The intrinsically topological flat bands, however, may be robust to this geometrical perturbation[19]. The difference in the size of the alternate triangles in the breathing kagome geometry may result in local electric dipole moments leading to ferroelectric order[21].

Angle-resolved photoemission spectroscopy (ARPES)[22–24] has served as a valuable technique allowing direct visualization of the band structure in quantum materials. In recent times, it has been successful in revealing the electronic structure of various kagome materials. Topological Dirac bands and/or flat bands in the electronic structures of Fe_3Sn_2[4,18,25], FeSn[14], CoSn[12,13], RT_6Sn_6(R = Tb, Y, Er, Ho, Gd, and T = Mn, V)[8,15,26–28], CsV_3Sb_5[29] have been observed by utilizing ARPES. A point to note is that most of these materials are metals with conventional kagome lattice, Fe_3Sn_2 with breathing kagome lattice reported in a recent ARPES study suggests a possibility of magnetic Weyl semimetallic phase in this material[25]. ARPES study of materials with the breathing kagome lattice is still limited. The Nb_3X_8 family of materials, where X = Cl, Br, I[30,31], provides material platforms to study the electronic structure arising from the breathing kagome geometry. Importantly, these materials have two-dimensional (2D) crystalline structures with very weak interlayer van der Waals interaction and hence can be thinned down to 2D limit via mechanical exfoliation[32–34]. They are semiconducting with a moderate band gap[33], which is suitable for electronic applications. In the monolayer limit, they are predicted to host ferromagnetic (FM) order[31,35,36], allowing a great platform to study the interplay among geometry, electronic correlations, and magnetism in 2D. Monolayer Nb_3I_8 is predicted to exhibit large spontaneous valley polarization making it suitable for valleytronics applications[37]. Systematic studies of the electronic structure of these semiconducting van der Waals breathing kagome materials are worthwhile, however, are lacking.

In this communication, via ARPES measurements, we report a systematic electronic structure study of breathing kagome semiconductor Nb_3I_8 assisted by density-functional theory (DFT) computations. Our experimental data is consistent with the semiconducting nature of Nb_3I_8 and reveals the presence of flat and weakly dispersing bands, that arise from the Nb-breathing kagome, in the electronic band structure of this material. These bands are observed to be sensitive to the polarization of the incident photon beam. The experimental observations are well reproduced by theoretical calculations. Our study provides a layered 2D material platform with flat bands thereby giving an opportunity to study the interaction among symmetry, geometry, electronic correlations, and potentially magnetism given the prediction of FM monolayer.

Results

Crystal structure and band calculations. Nb_3I_8 crystallizes in a trigonal crystal system with a rhombohedral space group $R\bar{3}m$ (number 166) with lattice parameters $a = b = 7.60$ Å and $c = 41.715$ Å[30]. A three-dimensional bulk crystal structure with six layers within a unit cell is shown in Fig. 1a where each layer along the crystallographic c-direction is connected through a weak van der Waals bond and within each layer, there is strong covalent bonding. The Nb atoms form a breathing kagome lattice with two distinct Nb–Nb distances in alternate Nb triangles and are sandwiched between the top and the bottom I-atom sheets, each containing two atomic layers (I1, I3 on the top sheet and I2, I4 on the bottom sheet) (see Supplementary Note 1 and Supplementary Fig. 1). The breathing kagome formed by the Nb-atoms can be seen in Fig. 1b, where each Nb atom has two long inter-triangular distances and two short intra-triangular distances with its four nearest neighbor Nb-atoms within the kagome plane. A schematic of the breathing lattice is presented in Fig. 1c, where the alternate triangles, unlike in a conventional kagome lattice, are not identical. Because of the presence of this special geometry in Nb_3I_8, flat bands are expected in its electronic structure. In Fig. 1d, a projected hexagonal BZ on (001) surface is presented with high-symmetry points and directions. In Fig. 1e, we present the calculated band structures for bulk Nb_3I_8 at $k_z = 0$. According to the calculation, Nb_3I_8 is semiconducting with a Kohn–Sham band gap (direct) of ~520 meV at the K point. Flat bands and weakly dispersing bands can be seen within 500 meV above and below the mid-gap. Such bands are present around 1 eV below the Fermi level as well. The overall frontier band structures of the bulk seem to be similar to that of the monolayer, indicating that the interlayer electronic couplings are weak (Supplementary Fig. 3 for monolayer calculation).

Experimental observation of flat bands. In Figs. 2–4, we present the electronic structure of Nb_3I_8 measured using ARPES. Nb_3I_8 is a semiconductor and the Fermi level lies within the gap. Therefore, no photoemission signal was observed at the Fermi level. ARPES signal is observed only about 300 meV below the Fermi level [see Fig. 2a]. Several pockets can be seen below 1 eV from the Fermi level, as shown in Fig. 2b. At a binding energy of about 1.6 eV, a nice hexagonal symmetry is observed in the energy contour [see Fig. 2c]. Next, in order to reveal the electronic structure of Nb_3I_8, we present the dispersion maps along various high-symmetry directions in Fig. 2d, e. The dispersion maps along $\overline{M} - \overline{\Gamma} - \overline{M}$ and $\overline{\Gamma} - \overline{K} - \overline{M} - \overline{K}$ show the presence of bands in accordance with the observations in the energy contours. The photoemission intensity is not uniform and especially at around 500 meV, is strongly suppressed out of a single BZ (also seen in Fig. 2a), possibly because of matrix element effects. This can be seen in the second derivative plot of the dispersion along $\overline{M} - \overline{\Gamma} - \overline{M}$, presented in Fig. 2f.

Next, we proceed to analyze the details of the bands observed along the high-symmetry directions along with a careful comparison with theoretically calculated bands using the DFT approach in Fig. 3. Figure 3a shows the dispersion map along $\overline{M} - \overline{\Gamma} - \overline{M}$ obtained from ARPES measurement using 90 eV photon energy. Around 500 meV below the Fermi level, there are two bands, one of which is almost flat (named B) and the other is weakly dispersing (named A), which correspond to the peaks in the integrated energy distribution curve (EDC) (Voigt fit) in Fig. 3b [also see Supplementary Fig. 9]. It has been predicted that flat and weakly dispersing bands in breathing kagome lattices might be intrinsically robust[19]. Another nearly flat band (named C) can also be observed below 1.2 eV binding energy. In Fig. 3c, we present the second derivative plot of the dispersion

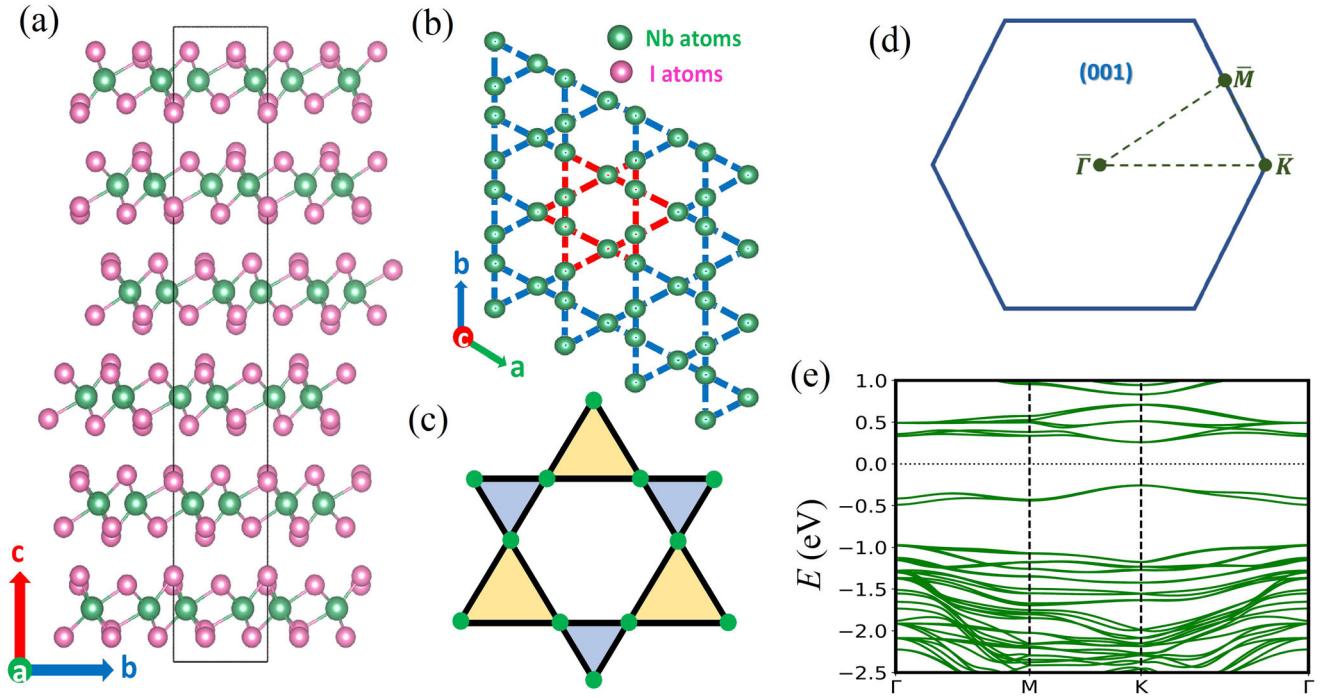

Fig. 1 Crystal structure and bulk band calculation of Nb_3I_8. a Crystal structure of Nb_3I_8, where the green and magenta spheres represent Nb and I atoms, respectively. **b** Nb atoms forming a breathing kagome lattice. A schematic of the breathing kagome lattice is presented in (**c**). The alternating triangles are not identical giving rise to a breathing lattice. **d** Projected hexagonal BZ on the (001) surface showing the high-symmetry points and directions. **e** Calculated band structure for bulk Nb_3I_8.

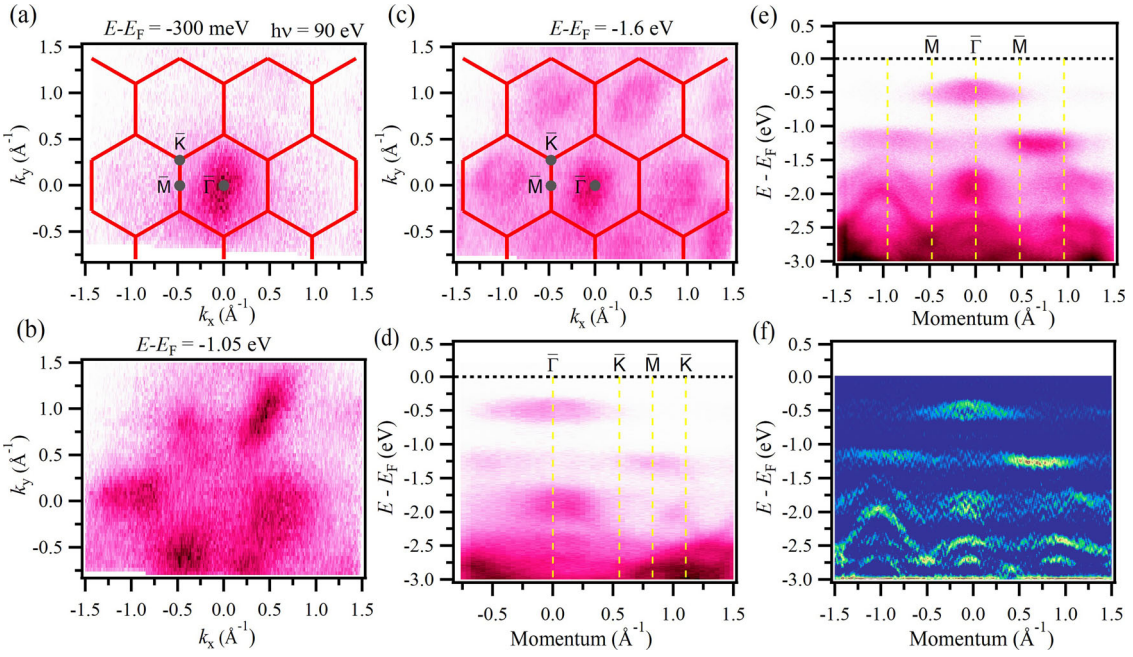

Fig. 2 ARPES measured energy contours (ECs) and band dispersions. a–c ECs at the binding energies of 300 meV, 1.05, and 1.6 eV, respectively. Red hexagons represent the BZ with high-symmetry points marked and labeled. **d** and **e** Band dispersions along different high-symmetry directions as shown in the plots. **f** Second derivative plot of (**e**). Data were collected at the ALS beamline 4.0.3 at a temperature of 260 K using a photon source of mono-energy 90 eV.

map in Fig. 3a, where the presence of two bands—one weakly dispersing (A) and the other almost flat (B)—can be clearly seen. Two minima peaks in the integrated EDC taken within (−0.5/Å–0/Å) of the second derivative plot (Fig. 3d) further confirm the presence of two bands. The minima peak exactly coincides with the maxima peaks in the integrated EDC in Fig. 3b. In Fig. 3e, f, we present the experimental band structure along $\overline{M}-\overline{\Gamma}-\overline{M}$ taken with 110 eV photon energy and calculated band structure using the DFT approach, respectively, where we can see a reasonable matching between the two. Within 500 meV of the mid-gap, the calculated data shows a set of almost flat bands (labeled as A and B) that have weak dispersions persisting down

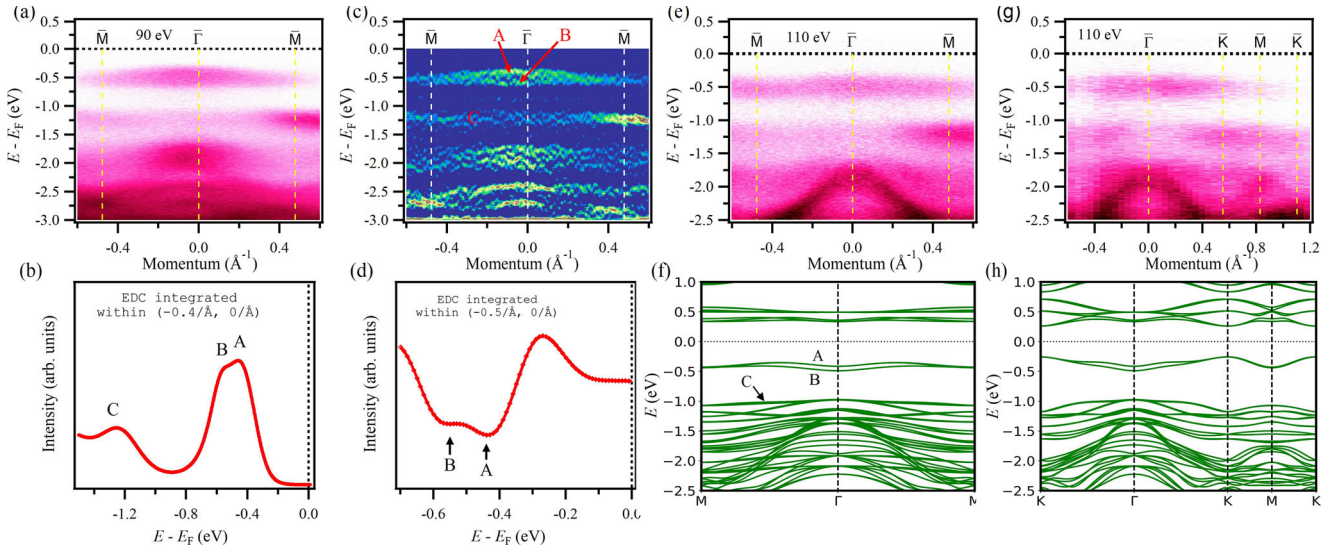

Fig. 3 Observation of flat and weakly dispersing bands. a, **b** ARPES measured band dispersions along $\overline{M} - \overline{\Gamma} - \overline{M}$ measured using photon energy of 90 eV and Integrated EDC (Voigt fit, also see Supplementary Note 6 and Supplementary Fig. 9) within a momentum window of (−0.4/Å-0/Å) in (**a**). **c**, **d** Second derivative plot of dispersion map in **a** and respective EDC curve taken within momentum window of (−0.5/Å-0/Å), respectively. **e** Experimental band dispersion along $\overline{M} - \overline{\Gamma} - \overline{M}$ direction. **f** Calculated bands along M−Γ−M. **g** Experimental band dispersion along the $\overline{\Gamma} - \overline{K} - \overline{M} - \overline{K}$ direction. **h** Calculated bands along Γ−K−M−K. ARPES data were collected at the ALS beamline 4.0.3 at a temperature of 260 K.

to the monolayer limit. Another set of almost flat bands (labeled C) appears around 1 eV below the Fermi level. Below C, DFT calculations show a continuum of band states consistent with the finite intensity observed in the experimental APRES spectra. The flat bands do not seem to vary their dispersion with the change in photon energy regardless of the variation in intensity, which possibly comes from the photoemission matrix element effect. This shows that these bands are of 2D nature, which is expected for 2D materials like Nb_3I_8 [For more variation in photon energy, see Supplementary Note 4 and Supplementary Fig. 7]. The dispersive bands below 1.5 eV binding energy, however, seem to strongly depend on the energy of the incident photon beam indicative of their 3D nature. Figure 3g, h represent the experimental and calculated band structures along $\overline{\Gamma} - \overline{K} - \overline{M} - \overline{K}$, respectively. The calculated result well reproduces the experimental observation.

Polarization dependence of the bands. In Fig. 4, we present the polarization dependence of the bands observed along the $\overline{M} - \overline{\Gamma} - \overline{M}$ direction. Polarization-dependent measurements have been performed at several photon energies including 120, 70, and 36 eV, and presented in Fig. 4a–c, respectively. It can be seen that the bands around 500 meV binding energy have strong intensity in the linear horizontal (LH) polarization [see bottom panel of Fig. 4d]. These bands are strongly suppressed in intensity when the incident photon beam is linear vertical (LV) polarized. With LV polarization, the intensity of the bands below 1.2 eV becomes strong [see top panel of Fig. 4d]. A weakly dispersing band can also be seen with LV polarized light [shown by the arrow in the right panels of Fig. 4a, c], supported by the two-peak feature in Fig. 4d top panel. In Fig. 4e, we present the contributions of Nb *d* and I *p* in the electronic structure of Nb_3I_8 along the $\overline{M} - \overline{\Gamma} - \overline{M}$ direction. It can be seen that the bands within 500 meV and just below 1 eV binding energy have a strong contribution from Nb *d* and the highly dispersive bands near the center of the BZ and below 1.5 eV are strongly dominated by I *p*. The flat bands observed in our experiments, therefore, originate from the breathing kagome lattice of the Nb atoms. We further perform orbital-resolved calculations to study the contribution of each *d* orbital, namely d_{zx}, $d_{x^2-y^2}$, d_{z^2}, d_{yz}, and d_{xy} [see Supplementary Note 5 and Supplementary Fig. 8 for orbital-resolved calculations]. The band sets A and B have strong contributions from d_{z^2} orbitals. On the other hand, the band sets C have significant contributions from all orbitals with the majority coming from the d_{xy} orbitals.

Discussion

Because of the breathing kagome geometry of the Nb atoms in Nb_3I_8, the Dirac fermion is not preserved in this system as in the case of the conventional kagome geometry. This might have led to the semiconducting nature of this material as seen in our theoretical calculations and backed by our experimental observation. However, the flat and weakly dispersing bands may remain robust despite the geometric perturbation from kagome to breathing kagome[19]. In our experimental measurements, we observe multiple flat and weakly dispersing bands at various binding energies. Our calculations also show that the frontier flat and weakly dispersing bands of the bulk are similar to those of the monolayer. This makes the choice of k_z not so significant in the measurements and can be validly compared with the DFT calculations (also see calculations for $k_z = 0$ and $k_z = \pi$ in Supplementary Fig. 5, where no significant differences can be seen). Our analysis shows that no band inversion occurs for the bands around 500 meV binding energy indicating non-topological character and quantized non-zero Chern numbers do not exist for the lower bands by rigidly shifting the Fermi level as they cannot be completely isolated in energy (see Supplementary Note 2 and Supplementary Fig. 4). Moreover, we can see in the experimental results that some bands, which are far below the Fermi level, depending on the choice of the photon energy (k_z value). This is expected because although Nb_3I_8 is a 2D material, the experimental sample is technically a three-dimensional bulk material. Importantly, our calculations show that the flat and weakly dispersing bands arise from the 2D breathing kagome plane of the Nb atoms.

In summary, we carried out ARPES measurements on a semiconducting kagome material Nb_3I_8 that can be exfoliated down to the 2D limit (see Supplementary Note 7 and

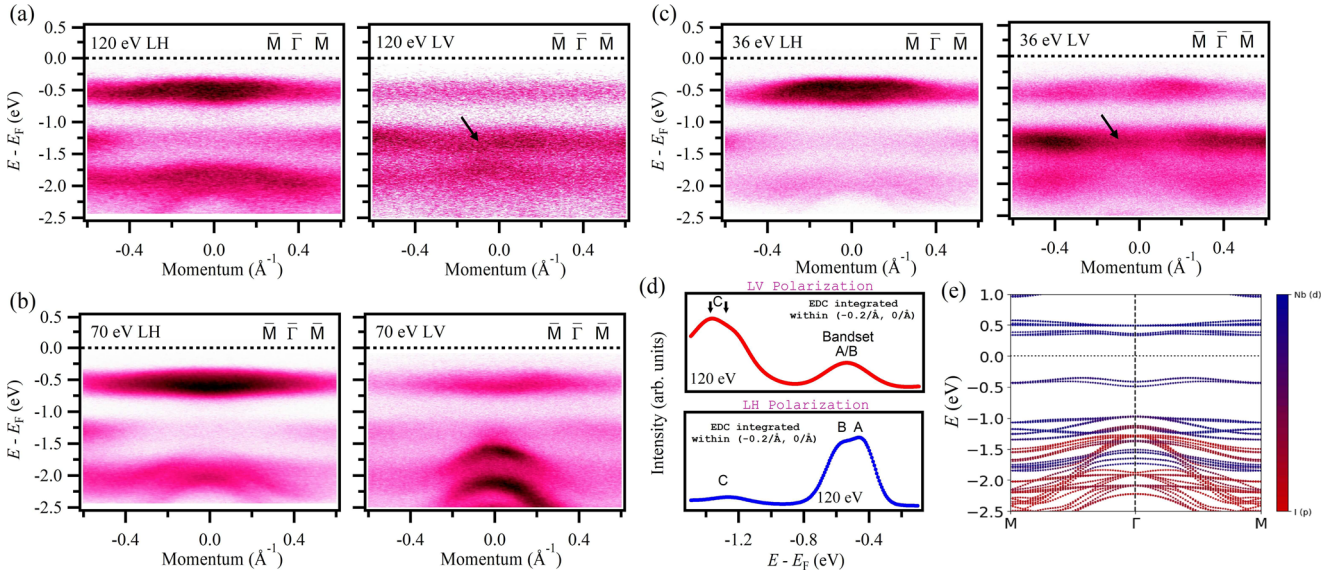

Fig. 4 Polarization-dependent band dispersion. a–c ARPES measured band dispersions along $\overline{M} - \overline{\Gamma} - \overline{M}$ measured using photon energies of 120, 70, and 36 eV, respectively, using LH or LV polarization as noted on each plot. **d** Fits of integrated EDCs (Voigt fits) taken within a momentum window of (−0.2/Å-0/Å) for 120 eV LH polarized (bottom) and LV polarized (top) data in (**a**) [also see Supplementary Fig. 9]. **e** Calculated orbital-resolved dispersion along M−Γ−M. ARPES data were collected at the ALS beamline 4.0.3 at a temperature of 260 K.

Supplementary Fig. 10) and discover flat as well as weakly dispersing bands that arise from the breathing kagome lattice of the Nb atoms. Computational results using DFT support our observation. These bands have 2D nature as expected for a 2D material based on our photon-energy-dependent measurements and show a strong dependence on the polarization of the photon beam. Our study points to Nb_3I_8 being an important ground to study the interplay among geometry and electronic correlations in 2D materials. Given that the monolayer of this compound is predicted to be FM and the exfoliation to stable few-layers to monolayer limit already reported to be achieved, it could throw magnetism as well in the mix.

Note. During the preparation of the manuscript, the authors became aware of similar work on a similar compound Nb_3Cl_8[38].

Methods

Crystal synthesis and characterization. High-quality single crystals of Nb_3I_8 were synthesized by utilizing the chemical vapor transport method (modified from a previously reported method[32]) using Iodine as a transport agent. 0.2303 g High purity Nb powder (99.99%, 325mesh from Alfa Aesar) and 0.8021 g Iodine (99.999% from Aldrich) were sealed inside a quartz tube (12.75 mm OD × 10.5 mm ID × 12 cm) under vacuum (<20 mTorr). The tube was loaded into a dual zone furnace and ramped for 20 h to reach 652 °C on the precursor side and 650 °C on the growth side. After 70 h growth, the tube and the furnace were allowed to naturally cool down to obtain flat and shiny crystals. The crystal structure was examined using X-ray diffraction and the chemical compositions of the obtained crystals were verified using scanning electron microscopy and energy-dispersive X-ray spectroscopy analysis (see Supplementary Fig. 2).

ARPES measurements. Synchrotron-based ARPES measurements were performed at the advanced light source (ALS) beamline 4.0.3 equipped with R8000 hemispherical analyzer. In order to obtain high-quality and fresh surfaces required for ARPES experiments, single crystals were cleaved in situ under ultra-high vacuum with pressure maintained in the order of 10^{-11} Torr. The measurements were carried out at a temperature of 260 K to evade charging effects. This leads to a thermal broadening of the bands in the ARPES spectra. LH and LV polarized photon sources in the range 30−124 eV were used during the measurements. For experimental geometry, see Supplementary Note 3 and Supplementary Fig. 6.

Computational methods. Computational results were obtained from first-principles calculations performed on the bulk stable state (antiferromagnetic, interlayer spin configuration with alternate layers having opposite spins) and monolayer stable state (FM) within the framework of DFT[39,40] as implemented in the QUANTUM ESPRESSO package[41]. Norm-conserving scalar relativistic Optimized Norm-Conserving Vanderbilt Pseudopotential (ONCVPSP)[42,43] and Perdew–Burke–Ernzerhof-type exchange-correlational functional[44] were used with van der Waals correction included in the D2 formalism[45]. A conventional unit cell with six layers with $a = 7.600$ Å and $c = 41.715$ Å[30] was used for the bulk calculations, and a single Nb_3I_8 layer with $c = 52.500$ Å was considered for monolayer calculations. Hubbard potential $U = 2$ eV on Nb d orbitals was used to account for the on-site interaction[31]. Note that the band structure calculations in Supplementary Fig. 5 are implemented in the Vienna Ab initio simulation package (VASP)[46]. For comparison with experimental data, we set the mid-band gap to be the zero-energy level. For more information, see Supplementary Note 2.

Data availability

The data supporting the findings of this study are available within the manuscript and the supplementary information. Other findings of this study are available from the corresponding author upon reasonable request.

Received: 18 March 2022; Accepted: 10 November 2022;
Published online: 16 December 2022

References

1. Kida, T. et al. The giant anomalous Hall effect in the ferromagnet Fe_3Sn_2-a frustrated kagome metal. *J. Phys. Condens. Mater.* **23**, 112205 (2011).
2. Han, T.-H. et al. Fractionalized excitations in the spin-liquid state of a kagome-lattice antiferromagnet. *Nature* **492**, 406 (2012).
3. Nakatsuji, S., Kiyohara, N. & Higo, T. Large anomalous Hall effect in a non-collinear antiferromagnet at room temperature. *Nature* **527**, 212 (2015).
4. Lin, Z. et al. Flatbands and emergent ferromagnetic ordering in Fe_3Sn_2 kagome lattices. *Phys. Rev. Lett.* **121**, 096401 (2018).
5. Yin, J.-X. et al. Giant and anisotropic many-body spin-orbit tunability in a strongly correlated kagome magnet. *Nature* **562**, 91 (2018).
6. Yin, J.-X. et al. Negative flat band magnetism in a spin–orbit-coupled correlated kagome magnet. *Nat. Phys.* **15**, 443 (2019).
7. Yang, S.-Y. et al. Giant, unconventional anomalous Hall effect in the metallic frustrated magnet candidate, KV_3Sb_5. *Sci. Adv.* **6**, eabb6003 (2020).
8. Yin, J.-X. et al. Quantum-limit Chern topological magnetism in $TbMn_6Sn_6$. *Nature* **583**, 533 (2020).
9. Lin, Z. et al. Dirac fermions in antiferromagnetic FeSn kagome lattices with combined space inversion and time-reversal symmetry. *Phys. Rev. B* **102**, 155103 (2020).
10. Ghimire, N. J. et al. Competing magnetic phases and fluctuation-driven scalar spin chirality in the kagome metal YMn_6Sn_6. *Sci. Adv.* **6**, eabe2680 (2020).

11. Mazin, I. I. et al. Theoretical prediction of a strongly correlated Dirac metal. *Nat. Commun.* **5**, 4261 (2014).
12. Liu, Z. et al. Orbital-selective Dirac fermions and extremely flat bands in frustrated kagome-lattice metal CoSn. *Nat. Commun.* **11**, 4002 (2020).
13. Kang, M. et al. Topological flat bands in frustrated kagome lattice CoSn. *Nat. Commun.* **11**, 4004 (2020).
14. Kang, M. et al. Dirac fermions and flat bands in the ideal kagome metal FeSn. *Nat. Mater.* **19**, 163 (2020).
15. Li, M. et al. Dirac cone, flat band and saddle point in kagome magnet YMn_6Sn_6. *Nat. Commun.* **12**, 3129 (2021).
16. Tang, E., Mei, J.-W. & Wen, X.-G. High-temperature fractional quantum Hall states. *Phys. Rev. Lett.* **106**, 236802 (2011).
17. Xu, G., Lian, B. & Zhang, S.-C. Intrinsic quantum anomalous Hall effect in the kagome lattice $Cs_2LiMn_3F_{12}$. *Phys. Rev. Lett.* **115**, 186802 (2015).
18. Ye, L. et al. Massive Dirac fermions in a ferromagnetic kagome metal. *Nature* **555**, 638 (2018).
19. Bolens, A. & Nagaosa, N. Topological states on the breathing kagome lattice. *Phys. Rev. B* **99**, 165141 (2019).
20. Ezawa, M. Higher-order topological insulators and semimetals on the breathing kagome and pyrochlore lattices. *Phys. Rev. Lett.* **120**, 026801 (2018).
21. Li, Y., Liu, C., Zhao, G.-D., Hu, T. & Ren, W. Two-dimensional multiferroics in a breathing kagome lattice. *Phys. Rev. B* **104**, L060405 (2021).
22. Damascelli, A., Hussain, Z. & Shen, Z.-X. Angle-resolved photoemission studies of the cuprate superconductors. *Rev. Mod. Phys.* **75**, 473 (2003).
23. Damascelli, A. Probing the electronic structure of complex systems by ARPES. *Phys. Scr.* **T109**, 61 (2004).
24. Lv, B., Qian, T. & Ding, H. Angle-resolved photoemission spectroscopy and its application to topological materials. *Nat. Rev. Phys.* **1**, 609 (2019).
25. Tanaka, H. et al. Three-dimensional electronic structure in ferromagnetic Fe_3Sn_2 with breathing kagome bilayers. *Phys. Rev. B* **101**, 161114 (2020).
26. Dhakal, G. et al. Anisotropically large anomalous and topological Hall effect in a kagome magnet. *Phys. Rev. B* **104**, L161115 (2021).
27. Kabir, F. et al. Unusual magnetic and transport properties in $HoMn_6Sn_6$ kagome magnet. *Phys. Rev. Mater.* **6**, 064404 (2022).
28. Peng, S. et al. Realizing kagome band structure in two-dimensional kagome surface states of RV_6Sn_6 (R = Gd, Ho). *Phys. Rev. Lett.* **127**, 266401 (2021).
29. Ortiz, B. R. et al. CsV_3Sb_5: a $\mathbb{Z}_2$ topological kagome metal with a superconducting ground state. *Phys. Rev. Lett.* **125**, 247002 (2020).
30. Magonov, S. N. et al. Scanning tunneling and atomic force microscopy study of layered transition metal halides Nb_3X_8 (X = Cl, Br, I). *J. Am. Chem. Soc.* **115**, 2495 (1993).
31. Jiang, J. et al. Exploration of new ferromagnetic, semiconducting and biocompatible Nb_3X_8 (X = Cl, Br or I) monolayers with considerable visible and infrared light absorption. *Nanoscale* **9**, 2992 (2017).
32. Kim, B. J. et al. Structural and electrical properties of Nb_3I_8 layered crystal. *Phys. Status Solidi RRL* **13**, 1800448 (2019).
33. Oh, S. et al. Large-area synthesis of van der Waals two-dimensional material Nb_3I_8 and its infrared detection applications. *J. Alloys Compd.* **831**, 154877 (2020).
34. Yoon, J. et al. Anomalous thickness-dependent electrical conductivity in van der Waals layered transition metal halide, Nb_3Cl_8. *J. Phys. Condens. Mater.* **32**, 304004 (2020).
35. Conte, F., Ninno, D. & Cantele, G. Layer-dependent electronic and magnetic properties of Nb_3I_8. *Phys. Rev. Res.* **2**, 033001 (2020).
36. Cantele, G., Conte, F., Zullo, L. & Ninno, D. Tunable electronic and magnetic properties of thin Nb_3I_8 nanofilms: interplay between strain and thickness. *Phys. Rev. B* **106**, 085418 (2022).
37. Peng, R. et al. Intrinsic anomalous valley Hall effect in single-layer Nb_3I_8. *Phys. Rev. B* **102**, 035412 (2020).
38. Sun, Z. et al. Observation of topological flat bands in the kagome semiconductor Nb_3Cl_8. *Nano Lett.* **22**, 4596 (2022).
39. Hohenberg, P. & Kohn, W. Inhomogeneous electron gas. *Phys. Rev.* **136**, B864 (1964).
40. Kohn, W. & Sham, L. J. Self-consistent equations including exchange and correlation effects. *Phys. Rev.* **140**, A1133 (1965).
41. Giannozzi, P. et al. QUANTUM ESPRESSO: a modular and open-source software project for quantum simulations of materials. *J. Phys. Condens. Mater.* **21**, 395502 (2009).
42. Hamann, D. R. Optimized norm-conserving Vanderbilt pseudopotentials. *Phys. Rev. B* **88**, 085117 (2013).
43. Hamann, D. R. Erratum: optimized norm-conserving Vanderbilt pseudopotentials [Phys. Rev. B 88, 085117 (2013)]. *Phys. Rev. B* **95**, 239906 (2017).
44. Perdew, J. P., Burke, K. & Ernzerhof, M. Generalized gradient approximation made simple. *Phys. Rev. Lett.* **77**, 3865 (1996).
45. Grimme, S. Semiempirical GGA-type density functional constructed with a long-range dispersion correction. *J. Comput. Chem.* **27**, 1787 (2006).
46. Kresse, G. & Furthmüller, J. Efficient iterative schemes for ab initio total-energy calculations using a plane-wave basis set. *Phys. Rev. B* **54**, 11169 (1996).

Acknowledgements

M.N. acknowledges the support from the National Science Foundation (NSF) CAREER award DMR-1847962, the Air Force Office of Scientific Research MURI Grant No. FA9550-20-1-0322, and NSF Partnerships for Research and Education in Materials (PREM) Grant DMR-2121953. X.X., T.C., J.-H.C., and J.Y. acknowledge the support from UW Molecular Engineering Materials Center, an NSF Materials Research Science and Engineering Center (Grant No. DMR-1719797). H.V. was supported by NSF PREM Grant DMR-2121953. This research used resources of the ALS, which is a DOE Office of Science User Facility under Contract No. DE-AC02-05CH11231.

Author contributions

M.N. and X.X. conceived the idea; M.N. supervised the project; X.X., J.-H.C., J.Y., and Y.Z. synthesized the samples and performed the characterization measurements; S.R. performed the experimental measurements with the help of A.P.S., G.D., J.D.D., I.B.E., and H.V.; T.C. and T.F. carried out the theoretical computations; S.R. analyzed the data; S.R. and M.N. made the figure plan and wrote the manuscript with contributions from all authors.

Competing interests

The authors declare no competing interests.

Additional information

Supplementary information The online version contains supplementary material available at https://doi.org/10.1038/s43246-022-00318-3.

Correspondence and requests for materials should be addressed to Madhab Neupane.

Peer review information *Communications Materials* thanks the anonymous reviewers for their contribution to the peer review of this work. Primary Handling Editors: Toru Hirahara and Aldo Isidori.

Reprints and permission information is available at http://www.nature.com/reprints

Publisher's note Springer Nature remains neutral with regard to jurisdictional claims in published maps and institutional affiliations.